

# Observing binary neutron star subpopulations with the Einstein Telescope

A. Toubiana<sup>1,2</sup> and I. Dvorkin<sup>3,4</sup>

<sup>1</sup> Dipartimento di Fisica “G. Occhialini”, Università degli Studi di Milano-Bicocca, Piazza della Scienza 3, 20126 Milano, Italy

<sup>2</sup> INFN, Sezione di Milano-Bicocca, Piazza della Scienza 3, 20126 Milano, Italy

<sup>3</sup> Institut d’Astrophysique de Paris, UMR 7095, CNRS and Sorbonne Université, 98 bis boulevard Arago, 75014 Paris, France

<sup>4</sup> Institut Universitaire de France, Ministère de l’Enseignement Supérieur et de la Recherche, 1 rue Descartes, 75231 Paris Cedex F-05, France

December 3, 2025

## ABSTRACT

**Aims.** The formation channels of binary neutron stars (BNSs) remain uncertain. The detection of GW190425 by LIGO/Virgo/KAGRA (LVK) suggests a subpopulation of massive BNSs, possibly formed through unstable “case BB” mass transfer with short merger delays. We investigate whether next-generation detectors such as the Einstein Telescope (ET) can identify and characterise such subpopulations.

**Methods.** Using the latest LVK constraints on the BNS merger rate, we generate mock ET catalogues containing a mixture of light and heavy subpopulations. The redshift distribution of each subpopulation is modeled as the convolution of the cosmic star formation rate with a time-delay distribution: heavy BNSs have fixed short delays, while light BNSs follow power-law delays with indices  $\alpha_L = -0.5, -1, -1.5$ . Hierarchical Bayesian analyses are then performed on catalogues of 100–5,000 events.

**Results.** With hundreds of detections from ET, we will be able to establish that the total mass distribution is bimodal. A few thousand events are sufficient to disentangle the redshift distributions of the two subpopulations for moderate time-delay indices ( $\alpha_L = -0.5$  or  $-1$ ). For steeper indices ( $\alpha_L = -1.5$ ), the differences are more subtle, requiring larger catalogues, beyond what we could explore given our computational resources.

**Conclusions.** Next-generation detectors should enable the detection of multiple BNS subpopulations and their redshift evolution, providing valuable insight into their formation pathways.

## 1. Introduction

Direct observations of binary neutron stars (BNSs) come primarily from radio observations of binary pulsars in the Milky Way (Özel & Freire 2016). The mass distribution of neutron stars (NSs) in these systems is found to be much narrower than that of the overall NS population (Alsing et al. 2018; Antoniadis et al. 2016; Farr & Chatziioannou 2020; Shao et al. 2020), and can be well described by a Gaussian distribution centered at  $1.33 M_\odot$  with a standard deviation of  $0.09 M_\odot$  (Ozel et al. 2012; Özel & Freire 2016), although there is some evidence of bimodality between recycled and non-recycled pulsars, the former having slightly larger masses (Farrow et al. 2019). This particularity of double radio pulsars could be attributed to the fact that the components of BNSs undergo much less accretion than neutron stars in other types of binaries, or to different masses at birth (Tauris et al. 2017).

Gravitational waves (GWs) provide a new means to directly observe these systems. The LIGO/Virgo/KAGRA (LVK) collaboration has so far confidently reported the detection of two BNSs: GW170817 (Abbott et al. 2017) and GW190425 (Abbott et al. 2020). While the masses of the NSs in GW170817 are in good agreement with those of the Galactic population, the masses of GW190425 are significantly higher than those of the local population. This discrepancy is particularly evident in terms of total mass:  $3.4^{+0.03}_{-0.01} M_\odot$  for GW190425, compared to  $2.66 \pm 0.12 M_\odot$  for the Galactic population.

This intriguing observation naturally raises the question of how GW190425 formed and why such heavy BNSs are not observed in the Milky Way. Dynamical formation in stellar clus-

ters could, in principle, produce heavier BNSs if a massive neutron star exchanges its stellar companion with another neutron star; however, this channel is expected to contribute negligibly to the overall BNS merger rate (Ye et al. 2020; Belczynski et al. 2018). Focusing on isolated binary evolution, some studies suggest that GW190425 could have formed through pathways similar to those of Galactic BNSs (Qin et al. 2024; Nair & Stevenson 2025), and that the spins and associated magnetic fields of heavy BNSs may render them effectively radio-invisible (Safarzadeh et al. 2020; Chu et al. 2025). Alternatively, Romero-Shaw et al. (2020) proposed that massive binaries like GW190425 may originate from a distinct evolutionary channel characterized by much shorter delays times between the formation of the progenitor stars and BNS merger, potentially explaining their scarcity in the Galaxy. In this scenario, the system undergoes unstable “case BB” mass transfer from a helium star onto the first-formed neutron star (Belczynski et al. 2002; Dewi & Pols 2003; Tauris et al. 2017; Vigna-Gómez et al. 2018; Iorio et al. 2023), triggering a second common-envelope phase between the neutron star and the remaining CO core. The resulting tighter orbital separation allows the binary to survive the second supernova kick and merge within a few million years. Following this idea, Galadage et al. (2021) jointly fitted the radio and GW BNS populations and found mild evidence that GW190425 could belong to a fast-merging population comprising 8–79% of all BNSs, with associated delay times between 5 and 401 Myr (assumed to be the same for all heavy BNSs).

If this hypothesis is correct, we could expect to observe two subpopulations of BNSs with GWs: a light population and

a heavy one, potentially exhibiting distinct redshift evolutions. While current GW detectors do not have the sensitivity necessary to distinguish between different subpopulations, next-generation ground-based observatories such as the Einstein Telescope (ET) (Branchesi et al. 2023; Abac et al. 2025a) and Cosmic Explorer (CE) (Evans et al. 2021, 2023), expected to come online by the end of the next decade, should detect thousands to tens of thousands of BNSs out to redshift  $z \sim 3$ . Using the latest constraints from the LVK on the local BNS merger rate (Abac et al. 2025b), we construct mock catalogues of BNS observations on which we perform hierarchical Bayesian analyses to reconstruct the astrophysical distributions. We find that approximately 500 events will be sufficient to identify the presence of two subpopulations, and a few thousand detections should allow us to distinguish their redshift distributions, highlighting the potential of next generation facilities to inform us on BNS formation.

## 2. Binary neutron star population

Our population model builds upon the works of Farrow et al. (2019) and Galaudage et al. (2021). In the latter, BNS systems are described as pairs composed of a recycled and a slowly spinning NS, each drawn from either a heavy (H) or a light (L) subpopulation. Here, we further assume that BNSs form preferentially as light/light or heavy/heavy, as it appears to be the case for GW170817 and GW190425. Under this assumption, the individual NS masses,  $m_1$  and  $m_2$ , associated with the heavy/light subpopulations are sampled from Gaussian distributions with means and standard deviations  $(\mu_{1,H/L}, \sigma_{1,H/L})$  and  $(\mu_{2,H/L}, \sigma_{2,H/L})$ , respectively. The numerical values of these parameters, adopted from Galaudage et al. (2021), are listed in Table 1.

In this formulation, no explicit ordering between  $m_1$  and  $m_2$  is imposed. To prevent labeling ambiguities that may arise in the GW context, we reparametrise the model in terms of the total mass  $m_t = m_1 + m_2$  and the mass ratio  $q = \min(m_1, m_2)/\max(m_1, m_2) \leq 1$ . The total mass is assumed to follow a normal distribution with a mean and standard deviation of  $\mu_{t,H/L} = \mu_{1,H/L} + \mu_{2,H/L}$  and  $\sigma_{t,H/L} = \sqrt{\sigma_{1,H/L}^2 + \sigma_{2,H/L}^2}$ , respectively. The mass ratio is modeled as a truncated log-normal distribution between 0 and 1, characterised by parameters  $\mu_{q,H/L}$  and  $\sigma_{q,H/L}$ . We show in App. A that this parametrisation results in a qualitatively similar distribution. Denoting by  $\lambda$  the fraction of light BNS, and by  $\Lambda = (\lambda, \Lambda_{t,L}, \Lambda_{q,L}, \Lambda_{z,L}, \Lambda_{t,H}, \Lambda_{q,H}, \Lambda_{z,H})$  the full set of population parameters, i.e. the hyperparameters, our population model reads:

$$p(m_t, q, z|\Lambda) = \lambda \times p(m_t|\Lambda_{t,L})p(q|\Lambda_{q,L})p(z|\Lambda_{z,L}) + (1 - \lambda) \times p(m_t|\Lambda_{t,H})p(q|\Lambda_{q,H})p(z|\Lambda_{z,H}). \quad (1)$$

The redshift distribution is given by

$$p(z|\Lambda_{z,H/L}) \propto \frac{1}{1+z} \frac{dV_c}{dz} \mathcal{R}_{H/L}(z). \quad (2)$$

Distributions are normalised between  $z_{\min} = 0$  and  $z_{\max} = 3$ , as we find that almost no BNS event is detected past redshift 3 with ET.  $\frac{dV_c}{dz}$  is the differential comoving volume, and  $\mathcal{R}_{H/L}(z)$  is the volumetric rate of events. The latter depends on the cosmic star formation rate (SFR), the BNS formation efficiency  $\eta_{H/L}$ , and the time-delay distribution  $p_{H/L}(\Delta t)$ :

$$\mathcal{R}_{H/L}(z) = \int \eta_{H/L}(t(z) + \Delta t) \text{SFR}(t(z) + \Delta t) p_{H/L}(\Delta t) d\Delta t. \quad (3)$$

Table 1: Parameters of our population models.

Parameter	Value
$\mu_{1,L}$	$1.34 M_\odot$
$\sigma_{1,L}$	$0.02 M_\odot$
$\mu_{2,L}$	$1.29 M_\odot$
$\sigma_{2,L}$	$0.09 M_\odot$
$\mu_{1,H}$	$1.47 M_\odot$
$\sigma_{1,H}$	$0.15 M_\odot$
$\mu_{2,H}$	$1.8 M_\odot$
$\sigma_{2,H}$	$0.15 M_\odot$
$\lambda$	0.5
$\lambda_R$	0.69; 0.56; 0.49
$\Lambda_{t,L}$	
$\mu_{t,L}$	$2.63 M_\odot$
$\sigma_{t,L}$	$0.092 M_\odot$
$\Lambda_{t,H}$	
$\mu_{t,H}$	$3.27 M_\odot$
$\sigma_{t,H}$	$0.21 M_\odot$
$\Lambda_{q,L}$	
$\mu_{q,L}$	1
$\sigma_{q,L}$	0.08
$\Lambda_{q,H}$	
$\mu_{q,H}$	0.82
$\sigma_{q,H}$	0.2
$\Lambda_{z,L}$	
$\Delta t_{\min,L}$	10 Myr
$\Delta t_{\max,L}$	13 Gyr
$\alpha_L$	-0.5; -1; -1.5
$\Lambda_{z,H}$	
$\Delta t_H$	30 Myr

**Notes.** The first eight lines list the parameters of the population model of Galaudage et al. (2021), which inspired our own. We then report the values of the hyperparameters used to generate the mock populations in our study, grouped by category. For completeness, we also provide the values of  $\lambda_R$  corresponding to the three choices of  $\alpha_L$  considered.

Following Romero-Shaw et al. (2020); Galaudage et al. (2021), we assume that the heavy subpopulation merges on shorter timescales than the light one. Accordingly, heavy binaries are assigned short, constant time delays of  $\Delta t_H = 30$  Myr, modeled as  $p_H(\Delta t) = \delta(\Delta t - \Delta t_H)$ , while light binaries are assumed to experience longer delays drawn from a power-law distribution with index  $\alpha_L$ , bounded between  $\Delta t_{L,\min} = 10$  Myr and  $\Delta t_{L,\max} = 13$  Gyr. We find that values of the lower cutoff of the power-law time-delay distribution,  $\Delta t_{L,\min}$ , and/or the fixed delay of the heavy population,  $\Delta t_H$ , below  $\sim 100$  Myr have a negligible impact on the resulting redshift distributions. Hence, the results presented below are largely insensitive to the precise choice of these parameters.

We adopt the cosmic SFR from Madau & Dickinson (2014). The formation efficiency of each subpopulation is assumed to be constant with redshift and thus acts as a normalisation factor. The overall normalisation is constrained by the total BNS merger rate

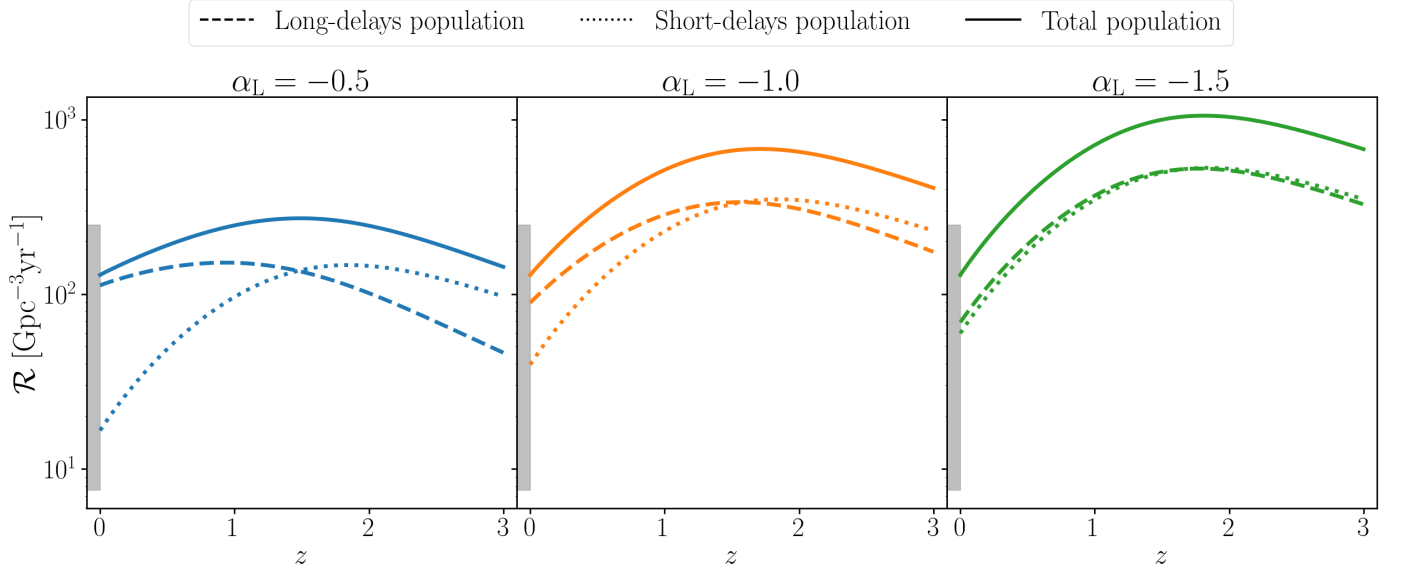


Fig. 1: Merger rate of the long delays population (dashed lines), short delays population (dotted lines) and total population (full line) for three different hypothesis of the time-delays distribution. The rate is normalised at  $z = 0$  to the mean of the interval reported by the LVK following GWTC-4 (Abac et al. 2025b). The gray band at  $z = 0$  shows the 90% credible interval reported by the LVK.

inferred by the LVK Collaboration (Abac et al. 2025b), while the relative contributions of each subpopulation are set by the choice of the mixing fraction  $\lambda$ . We emphasise that the mixing fraction entering the probability density function,  $\lambda$ , differs from the one entering the volumetric rate,  $\lambda_{\mathcal{R}}$ . Defining the latter such that  $\mathcal{R}(z) = \lambda_{\mathcal{R}}\mathcal{R}_L(z) + (1 - \lambda_{\mathcal{R}})\mathcal{R}_H(z)$ , the two are related by

$$\lambda_{\mathcal{R}} = \frac{\lambda \int_{z_{\min}}^{z_{\max}} \frac{\mathcal{R}_H(z)}{1+z} \frac{dV_c}{dz} dz}{\int_{z_{\min}}^{z_{\max}} \frac{\lambda \mathcal{R}_L(z) + (1-\lambda)\mathcal{R}_H(z)}{1+z} \frac{dV_c}{dz} dz}. \quad (4)$$

Here, we assume an equal contribution from both populations, i.e.  $\lambda = 0.5$ . We summarise the parameters of our population in Table 1. For completeness, we also report there the corresponding values of  $\lambda_{\mathcal{R}}$ . Our values are compatible with the estimates of Galaudage et al. (2021) that 8-79% of BNS at birth would be rapidly merging (in terms of  $\lambda_{\mathcal{R}}$ ).

Since the time-delay distribution is poorly constrained, we explore different assumptions for the delay-time distribution of the slowly merging (light) population. Specifically, we fix the minimum and maximum values of the time-delay range and vary the power-law index  $\alpha_L$ . Population synthesis models typically find  $\alpha_L = -1$  (e.g. Chruslinska et al. 2018), although at specific progenitor metallicities the distribution can be much more shallow (de Sá et al. 2024; Pellouin et al. 2025), while observational-based estimates that use gamma-ray bursts or Galactic pulsars find much steeper values of  $\alpha_L = -1.5$  to  $-2$  for some subpopulations (Zevin et al. 2022; Maoz & Nakar 2025). In this work we consider  $\alpha_L = -0.5, -1, \text{ and } -1.5$ . The corresponding volumetric merger rates are shown in Fig. 1.

In each case, the total rate is normalised to the mean of the 90% credible interval on the local BNS merger-rate range reported by the LVK (Abac et al. 2025b), between 7.6 and 250  $\text{Gpc}^{-3}\text{yr}^{-1}$ , i.e. 129  $\text{Gpc}^{-3}\text{yr}^{-1}$ . The gray band at  $z = 0$  shows the credible interval reported by the LVK. The short-delay population is rescaled by a normalisation factor for each model, since for a fixed  $\lambda$ , the corresponding volumetric-rate mixing fraction  $\lambda_{\mathcal{R}}$  depends on  $\alpha_L$ . Larger values of  $\alpha_L$  assign greater weight to long delays, thereby enhancing the contrast with the short-delay population.

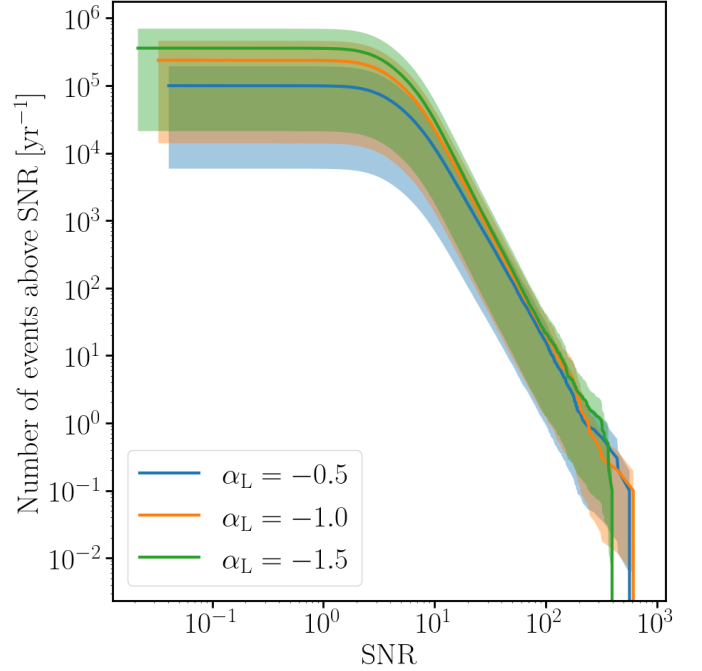


Fig. 2: Number of events above a given SNR threshold per year in the three scenarios considered for the time-delay distribution.

### 3. Mock catalogues and data analysis

We consider a triangular configuration for ET with 10 km arm length and adopt the ET-10 (10 km-xylophone) sensitivity curve (Danilishin & Zhang 2023) implemented in GWBENCH (Borhanian 2021). Our mock detection and parameter estimation pipeline is based on the approach outlined in Fishbach et al. (2020); Farah et al. (2023). Differences arising in our implementation are discussed in App. B.

Figure 2 shows the cumulative number of detections as a function of SNR threshold for the three values of  $\alpha_L$ . The shaded

regions represent the uncertainty associated with the local BNS merger rate reported by the LVK (Abac et al. 2025b), corresponding to the lower and upper bounds of the 90% credible interval. Assuming an SNR threshold of 8, we estimate that ET will detect between approximately 1,180–38,920, 2,370–77,950, and 3,320–109,150 BNS mergers per year for  $\alpha_L = -0.5$ ,  $-1$ , and  $-1.5$ , respectively. In all cases,  $\sim 93\%$  of detected BNS are within redshift 2. These estimates are compatible with Branchesi et al. (2023) after accounting for the fact that they assumed a local merger rate of  $250 \text{ Gpc}^{-3} \text{ yr}^{-1}$ , which lies at the higher end of our range.

Based on these projections, we generate mock catalogues containing 100, 500, 1,000, and 5,000 detected events, with 10 realisations for each case. We then perform hierarchical Bayesian inference to recover the population hyperparameters. These catalogue sizes are consistent with the expected ET detection rate, towards its lower end, while remaining computationally tractable. Current computational resources, in terms of both processing time and memory requirements, prevent us from extending the analysis to the tens of thousands of detections that ET is expected to observe. For this reason, we restrict our study to catalogues of up to 5,000 events. The hierarchical Bayesian framework is described in detail in App. C; here, we summarise the population modelling choices relevant to this work.

Our population prior is given by a mixture model as in Eq. (1). The component distributions in total mass and mass ratio are modeled as Gaussian and truncated log-normal distributions, respectively. We adopt flat priors on the mixture fraction, as well as on the means and standard deviations of these distributions. For the redshift dependence, we explore two complementary approaches.

We assume that the redshift evolution of each subpopulation follows Eqs. (2) and (3). In the inference, we model the delay-time distribution of both subpopulations as a power-law, i.e., we do not assume any of them to have a fixed delay time. The delta-function limit is recovered when  $\Delta t_{\text{max}} \rightarrow \Delta t_{\text{min}}$ . The priors adopted are:

- $\Delta t_{\text{min}}$ : log-flat between 1 Myr and 1 Gyr;
- $\Delta t_{\text{max}} - \Delta t_{\text{min}}$ : log-flat between  $10^{-3}$  Myr and  $13.5 \text{ Gyr}^1$ ;
- $\alpha$ : flat between  $-3$  and  $0$ .

After performing the hierarchical Bayesian inference, we compute the probability that the mass distribution is bimodal,  $p_{\text{bimodal}}$ , as follows. For each hyperposterior sample, we draw 2,000  $(m_t, q)$  samples and apply Hartigan’s dip test (Hartigan & Hartigan 1985) using the implementation of Urlus (2025). This test quantifies whether the empirical probability distribution function of the samples exhibits a “dip,” which would indicate the presence of two distinct modes. The test returns a  $p$ -value that can be interpreted as the probability that the distribution is unimodal. Repeating this for all hyperposterior samples yields a distribution of  $p$ -values for each hierarchical Bayesian analysis. We then compute  $p_{\text{bimodal}}$  as the fraction of  $p$ -values below 0.05, which provides an estimate of the probability that the mass distribution is bimodal with more than 95% confidence. We verified that the number of  $(m_t, q)$  samples drawn per hyperparameter sample is sufficient, in the sense that increasing it does not affect the results. Since Hartigan’s dip test is defined for one-dimensional data, we rotate the  $(m_t, q)$  samples for each hyperposterior draw using a rotation matrix, and retain the rotation that yields the lowest  $p$ -value (i.e., the highest probability

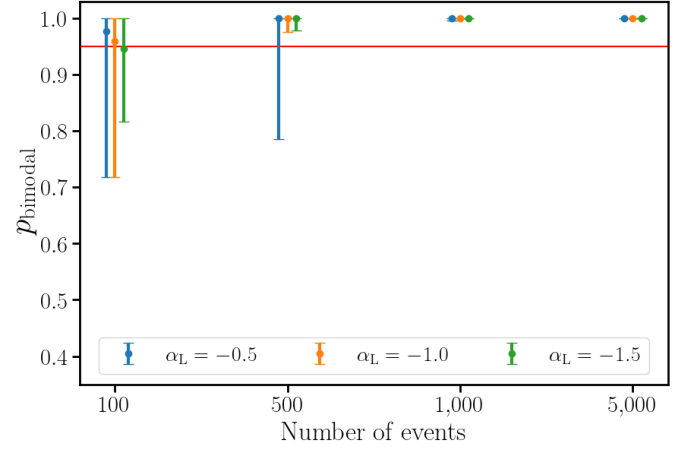


Fig. 3: Credible intervals on the confidence that the mass distribution is bimodal as a function of the number of events and for the different values of  $\alpha_L$ . The red horizontal line corresponds to a probability of 0.95.

of bimodality). This procedure allows us to identify which linear combination of  $m_t$  and  $q$  exhibits the strongest bimodality. In practice, we find that the angle maximising the bimodality is approximately zero, indicating that the total mass distribution itself is the main source of bimodality.

The probability that the two redshift distributions are different,  $p_{\text{dist}}$ , is estimated as follows. We randomly draw pairs of hyperparameters from the posterior samples and compute the Kolmogorov–Smirnov (KS) statistic between the resulting redshift distributions of the two subpopulations. This “between-population” KS distribution captures the typical differences between the two sets of distributions. To construct a background distribution, we also compute two “within-population” KS distributions by comparing different samples from the same subpopulation, providing a reference for variations expected from measurement uncertainty (detector noise and finite number of events). We then determine the 5% quantile of the “between-population” KS distribution and find its corresponding quantiles in the “within-population” KS distributions. The maximum of these two quantiles is defined as  $p_{\text{dist}}$ . It measures whether the difference between the subpopulations exceeds the typical measurement-induced variations in at least one subpopulation, indicating that the distributions can be reliably distinguished.

## 4. Results

We start by discussing the recovery of the mass distribution. Already with 100 events, we can confidently measure that  $\lambda \neq 0$  and  $\lambda \neq 1$ , indicating that the population cannot be described by a single component. In App. D we show examples of how the total mass and mass ratio distributions are recovered as the number of events increases. Figure 3 displays the 90% confidence interval of  $p_{\text{bimodal}}$  (centered on the median) as a function of the number of events. With 500 detections, we can already establish in most cases that the total mass distribution is bimodal, and with 1,000 detections this can be determined unambiguously, regardless of  $\alpha_L$ .

Next, we turn to the distinction between the two redshift distributions. The upper panel of Fig. 4 shows representative examples of the reconstructed redshift distributions for  $\alpha_L = 1$  as the number of events increases. The lower panel shows the dis-

<sup>1</sup> The limit  $\Delta t_{\text{max}} = \Delta t_{\text{min}}$  is not included in our prior; however, intervals shorter than 1 Myr are in practice hardly distinguishable from a delta function.

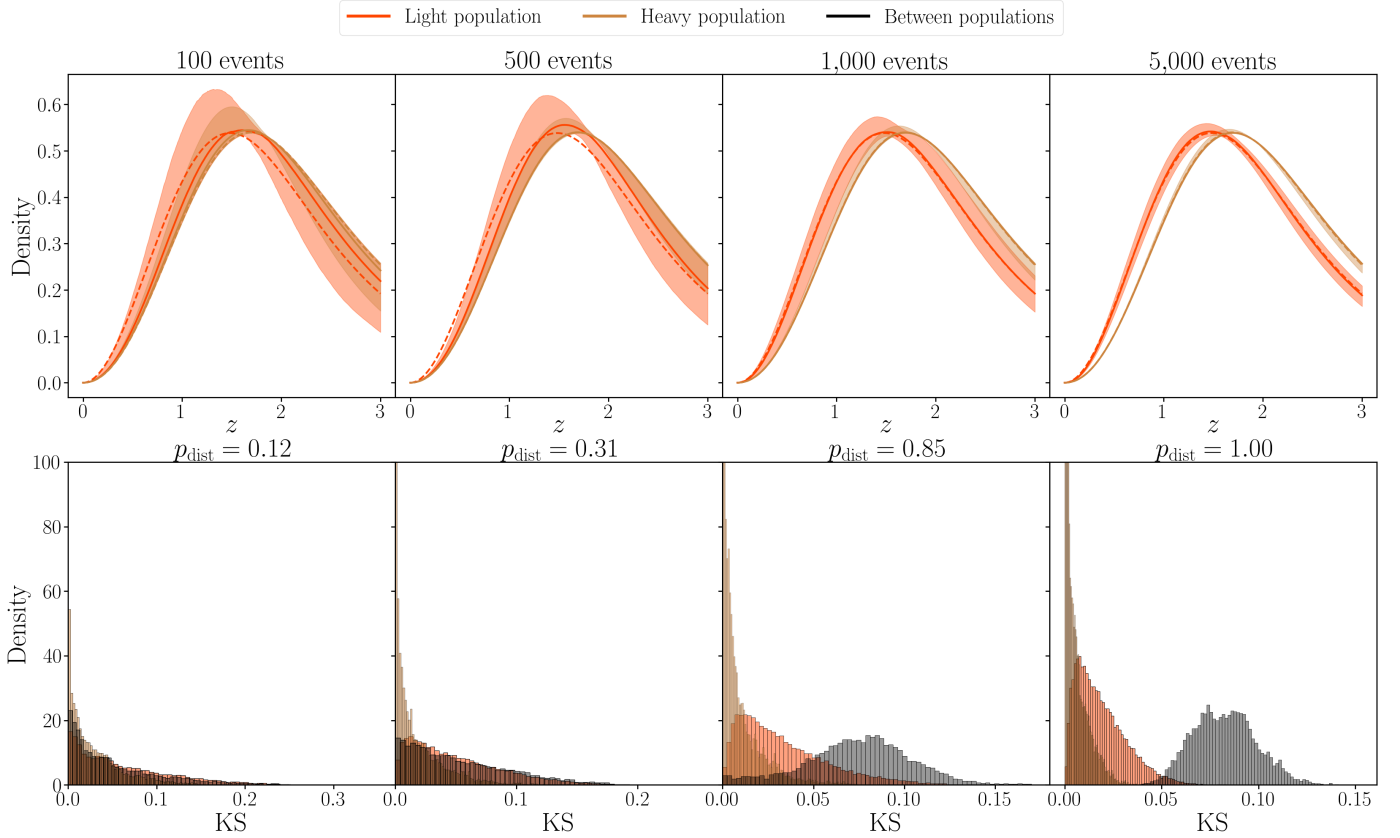


Fig. 4: Upper panel: reconstructions of the redshift distributions for increasing catalogue sizes. Coloured bands show the 90% credible intervals for the light (red) and heavy (golden) populations. Solid lines indicate the median reconstructions, while dashed lines mark the true distributions. For the heavy population, the dashed and full lines superimpose almost perfectly. Lower panel: distribution of within-population and between-populations KS statistics. The value on top shows the probability that the two heavy and light population have different redshift distributions.

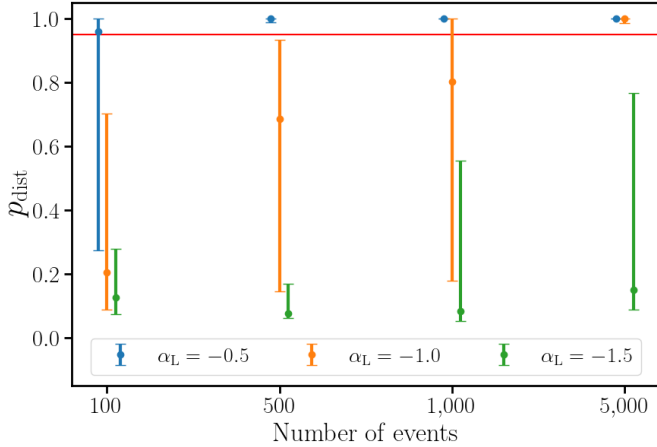


Fig. 5: Credible intervals on the confidence with which we can determine that the redshift distribution of the light and of the heavy population are different as a function of the number of events and for the different values of  $\alpha_L$ . The red horizontal line corresponds to a probability of 0.95.

tribution of KS statistics, both between-population and within-population. The value above the bottom panel indicates  $p_{\text{dist}}$ . This figure provides a visual interpretation of our method for estimating the probability that the two redshift distributions dif-

fer: as the confidence bands overlap less, the between-population KS distribution is moved towards higher values than the within-population ones, and the computed  $p_{\text{dist}}$  increases. We observe that the redshift distribution of the heavy population is typically better constrained than that of the light population, as a consequence of their larger SNR.

Our results for  $p_{\text{dist}}$  are shown in Fig. 5. For  $\alpha_L = -0.5$ , we can already establish that the two redshift distributions differ with more than 95% confidence using 1,000 events. For  $\alpha_L = -1$ , this level of significance is reached in over 95% of realisations with 5,000 events. For  $\alpha_L = -1.5$ , the distinction becomes more challenging, and it appears that many more events are needed in order to distinguish the distributions.

## 5. Conclusions

The formation pathway of BNSs remains largely unconstrained. Different assumptions on mass transfer lead to widely varying predicted populations, and the detection of GW190425 by the LVK highlighted the possibility that a significant fraction of BNSs form through unstable “case BB” mass transfer, with much shorter time delays than the rest of the population (Romero-Shaw et al. 2020; Galadage et al. 2021). In this scenario, two BNS subpopulations with distinct redshift evolutions could coexist. In this paper, we explore the ability of future ground-based facilities such as ET to probe this possibility.

Using the latest estimate of the BNS merger rate by the LVK (Abac et al. 2025b), we generated mock BNS populations consisting of an equal mixture of light and heavy subpopulations, inspired by the parametric models of Farrow et al. (2019); Galaudage et al. (2021). Assuming that the redshift distribution of each subpopulation is given by the convolution of the SFR with a time-delay distribution, we adopted a fixed, short time delay for heavy BNSs, while for light BNSs we assumed a power-law distribution with indices  $\alpha_L = -0.5, -1, -1.5$ . Independently of this choice, we find that ET should observe at least a few thousand BNS mergers over its lifetime, with estimated detection rates ranging from 2,370 to 77,950 events per year in the fiducial  $\alpha_L = -1$  case.

We then considered multiple realisations of catalogues ranging from 100 up to 5,000 events and performed hierarchical Bayesian analyses to reconstruct the astrophysical distributions. Crucially, in the inference, we did not constrain either subpopulation to a fixed delay time, allowing for a more general and flexible model. For all  $\alpha_L$  values, we find that with 500 events we can identify the bimodality of the BNS total-mass distribution in most cases, and with 1,000 events we can do so essentially always. Moreover, a few thousand events are sufficient to disentangle the redshift distributions of the two subpopulations if  $\alpha_L = -0.5$  or  $-1$ . For  $\alpha_L = -1.5$ , the difference between the two distributions is very small, and more observations would be required to distinguish them, if at all. We could not explore this further due to limited computational resources. This highlights a crucial point: current population analysis frameworks will face significant challenges when the number of observations reaches several thousand.

Our study shows that next-generation ground-based detectors could reveal a subpopulation of heavy BNSs merging on much shorter timescales than the Galactic population. The most likely scenario behind it would be unstable “case BB” mass transfer, which tightens the binary orbit, allowing the system to remain bound after the second supernova and resulting in shorter merger delays. Detecting such a population would provide unique insight into BNS formation channels, accessible only through GW observations, since rapidly merging heavy BNSs would be largely absent in the Milky Way, explaining the lack of Galactic binaries as massive as GW190425. Alternatively, if heavy BNSs exist in our Galaxy, but are radio-invisible (Safarzadeh et al. 2020; Chu et al. 2025), the Laser Interferometer Space Antenna (LISA) should allow to find them in the Milky Way (Korol & Safarzadeh 2021).

An important caveat of our analysis is that it was limited to two subpopulations. For instance, allowing for a light/heavy coupling would introduce a third subpopulation, although the (currently limited) data tend to favour mostly heavy/heavy and light/light coupling. Moreover, several formation pathways may contribute to the BNS population (Tauris et al. 2017; Vigna-Gómez et al. 2018), potentially resulting in a more complex distribution. Neglecting this could severely bias population reconstruction when using parametric or astrophysical models for the population prior (Zevin et al. 2021; Toubiana et al. 2021). Future work will explore more comprehensive analyses combining population synthesis models (Pellouin et al. 2025) with multi-dimensional non-parametric approaches, such as the one of Tenorio et al. (2025).

**Acknowledgements.** We are thankful to S. Borhanian, T. Bruel and M. for fruitful discussions. A.T. is supported by MUR Young Researchers Grant No. SOE2024-0000125, ERC Starting Grant No. 945155–GWmining, Cariplo Foundation Grant No. 2021-0555, MUR PRIN Grant No. 2022-Z9X4XS, Italian-French University (UIF/UIFI) Grant No. 2025-C3-386, MUR Grant “Progetto Diparti-

menti di Eccellenza 2023-2027” (BiCoQ), and the ICSC National Research Centre funded by NextGenerationEU

## References

- Abac, A. et al. 2025a [arXiv:2503.12263]  
 Abac, A. G. et al. 2025b [arXiv:2508.18083]  
 Abbott, B. P. et al. 2017, Phys. Rev. Lett., 119, 161101  
 Abbott, B. P. et al. 2020, Astrophys. J. Lett., 892, L3  
 Alsing, J., Silva, H. O., & Berti, E. 2018, Mon. Not. Roy. Astron. Soc., 478, 1377  
 Antoniadis, J., Tauris, T. M., Ozel, F., et al. 2016 [arXiv:1605.01665]  
 Belczynski, K., Kalogera, V., & Bulik, T. 2002, ApJ, 572, 407  
 Belczynski, K. et al. 2018, Astron. Astrophys., 615, A91  
 Borhanian, S. 2021, Class. Quant. Grav., 38, 175014  
 Branchesi, M. et al. 2023, JCAP, 07, 068  
 Chruslinska, M., Belczynski, K., Klencki, J., & Benacquista, M. 2018, Mon. Not. Roy. Astron. Soc., 474, 2937  
 Chu, Q., Lu, Y., & Yu, S. 2025, Astrophys. J., 980, 181  
 Danilishin, S. & Zhang, T. 2023, ET sensitivity curves used for CoBA Science Study, Technical Report ET-0304B-22, Einstein Telescope Collaboration  
 de Sá, L. M., Rocha, L. S., Bernardo, A., Bachega, R. R. A., & Horvath, J. E. 2024, Mon. Not. Roy. Astron. Soc., 535, 2041  
 Dewi, J. D. M. & Pols, O. R. 2003, MNRAS, 344, 629  
 Essick, R. 2023, Phys. Rev. D, 108, 043011  
 Evans, M. et al. 2021 [arXiv:2109.09882]  
 Evans, M. et al. 2023 [arXiv:2306.13745]  
 Farah, A. 2022, GWMockCat: A lightweight code to generate mock catalogs of gravitational-wave sources, <https://git.ligo.org/amanda.farah/GWMockCat>, gitLab repository, release v1 (May 03, 2022)  
 Farah, A. M., Edelman, B., Zevin, M., et al. 2023, Astrophys. J., 955, 107  
 Farr, W. M. & Chatziioannou, K. 2020, Research Notes of the American Astronomical Society, 4, 65  
 Farrow, N., Zhu, X.-J., & Thrane, E. 2019, Astrophys. J., 876, 18  
 Finn, L. S. & Chernoff, D. F. 1993, Phys. Rev. D, 47, 2198  
 Fishbach, M., Farr, W. M., & Holz, D. E. 2020, Astrophys. J. Lett., 891, L31  
 Galaudage, S., Adamcewicz, C., Zhu, X.-J., Stevenson, S., & Thrane, E. 2021, Astrophys. J. Lett., 909, L19  
 García-Quirós, C., Colleoni, M., Husa, S., et al. 2020, Phys. Rev. D, 102, 064002  
 Gerosa, D. & Bellotti, M. 2024, Class. Quant. Grav., 41, 125002  
 Hartigan, J. & Hartigan, P. 1985, Annals of Statistics, 13, 70  
 Iorio, G. et al. 2023, Mon. Not. Roy. Astron. Soc., 524, 426  
 Karnesis, N., Katz, M. L., Korsakova, N., Gair, J. R., & Stergioulas, N. 2023, Mon. Not. Roy. Astron. Soc., 526, 4814  
 Korol, V. & Safarzadeh, M. 2021, Mon. Not. Roy. Astron. Soc., 502, 5576  
 Madau, P. & Dickinson, M. 2014, Ann. Rev. Astron. Astrophys., 52, 415  
 Mandel, I., Farr, W. M., & Gair, J. R. 2019, Mon. Not. R. Astron. Soc., 486, 1086  
 Maoz, D. & Nakar, E. 2025, Astrophys. J., 982, 179  
 Nair, A. & Stevenson, S. 2025 [arXiv:2508.15624]  
 Özel, F. & Freire, P. 2016, Ann. Rev. Astron. Astrophys., 54, 401  
 Ozel, F., Psaltis, D., Narayan, R., & Villarreal, A. S. 2012, Astrophys. J., 757, 55  
 Pellouin, C., Dvorkin, I., & Lehoucq, L. 2025, Astron. Astrophys., 693, A283  
 Qin, Y. et al. 2024, Astron. Astrophys., 691, A214  
 Regimbau, T. et al. 2012, Phys. Rev. D, 86, 122001  
 Romero-Shaw, I. M., Farrow, N., Stevenson, S., Thrane, E., & Zhu, X.-J. 2020, Mon. Not. Roy. Astron. Soc., 496, L64  
 Safarzadeh, M., Ramirez-Ruiz, E., & Berger, E. 2020, Astrophys. J., 900, 13  
 Shao, D.-S., Tang, S.-P., Jiang, J.-L., & Fan, Y.-Z. 2020, Phys. Rev. D, 102, 063006  
 Talbot, C. & Golomb, J. 2023, Mon. Not. R. Astron. Soc., 526, 3495  
 Tauris, T. M. et al. 2017, Astrophys. J., 846, 170  
 Tenorio, R., Toubiana, A., Bruel, T., Gerosa, D., & Gair, J. R. 2025, Astrophys. J. Lett., 994, L52  
 Toubiana, A., Wong, K. W. K., Babak, S., et al. 2021, Phys. Rev. D, 104, 083027  
 Urlus, R. 2025, diptest: Hartigan’s dip test for unimodality (Python/C++), python package implementing Hartigan and Hartigan’s dip test for unimodality  
 Vigna-Gómez, A., Neijssel, C. J., Stevenson, S., et al. 2018, MNRAS, 481, 4009  
 Vitale, S., Gerosa, D., Farr, W. M., & Taylor, S. R. 2020, in Handbook of Gravitational Wave Astronomy (Springer)  
 Ye, C. S., Fong, W.-f., Kremer, K., et al. 2020, Astrophys. J. Lett., 888, L10  
 Zevin, M., Bavera, S. S., Berry, C. P. L., et al. 2021, Astrophys. J., 910, 152  
 Zevin, M., Nugent, A. E., Adhikari, S., et al. 2022, Astrophys. J. Lett., 940, L18

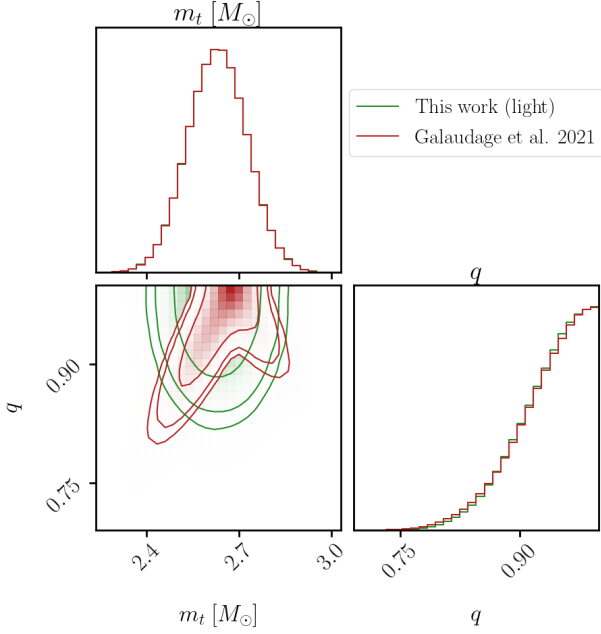


Fig. A.1: Comparison between the parametrisation of Galaudage et al. (2021) for the light population and ours in terms of total mass and mass ratio.

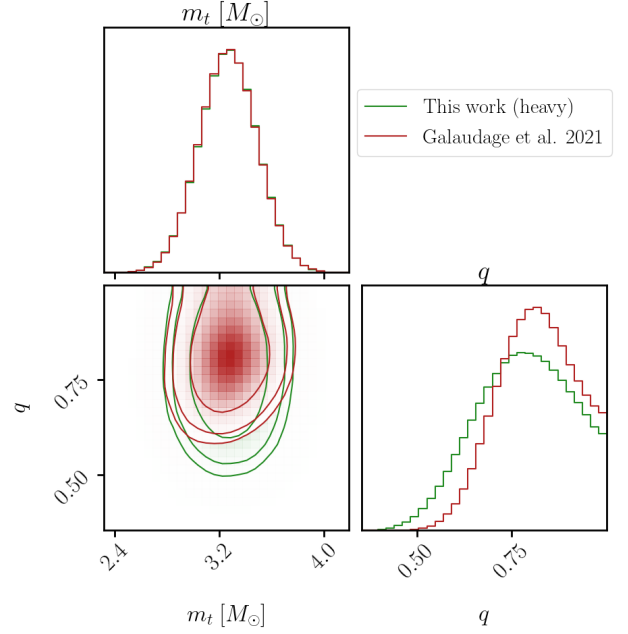


Fig. A.2: Comparison between the parametrisation of Galaudage et al. (2021) for the heavy population of ours in terms of total mass and mass ratio.

## Appendix A: Comparison between population parametrisations

Figures A.1 and A.2 compare our population model with that of Galaudage et al. (2021), with the extra condition that only light/light and heavy/heavy pairings are allowed. The total mass distributions are identical, as both models describe them as the sum of two Gaussians. The corresponding mass-ratio distributions are qualitatively similar. The discontinuity visible in the  $(m_t, q)$  correlation for the light population originates from the fact that in Galaudage et al. (2021), the component masses are not ordered; enforcing  $q \leq 1$  thus introduces this artificial feature. Still, our model has a similar support to the original distribution.

## Appendix B: Mock detection and parameter estimation

In their appendices, Fishbach et al. (2020) and Farah et al. (2023) outline a prescription for generating mock gravitational-wave (GW) catalogues that self-consistently incorporate parameter estimation uncertainty and selection effects, while also reproducing the expected scaling of measurement errors with the inverse of the signal-to-noise ratio (SNR). Their approach leverages the fact that the SNR,  $\rho$ , can be written as

$$\rho = \frac{F(\theta')}{D_L}, \quad (\text{B.1})$$

where  $\theta'$  denotes all binary parameters entering the SNR computation except for the luminosity distance  $D_L$  (detector frame masses, spins, sky location...). For fixed  $\theta'$ , this expression allows one to transform straightforwardly between  $D_L$  and  $\rho$ .

The key idea is to treat the SNR itself as a sampling parameter during mock parameter estimation, rather than the luminosity distance. This makes it possible to enforce that the measured

SNR,  $\tilde{\rho}$ , is normally distributed around the true SNR, with unit variance:  $\tilde{\rho} \sim \mathcal{N}(\rho, 1)$ , which reflects the expected behaviour of a matched-filter SNR in the case of a single detector (Finn & Chernoff 1993). Selection effects are then included as follows: for each source, the true SNR is computed and scattered according to the above distribution to obtain  $\tilde{\rho}$ ; the event is retained only if  $\tilde{\rho}$  exceeds a chosen SNR threshold,  $\rho_{\text{th}}$ .

For retained events, posterior samples of the SNR,  $\hat{\rho}$ , are then drawn from a normal distribution centred at  $\tilde{\rho}$  with unit variance. To model measurement uncertainty on the remaining parameters  $\theta'$ , “noisy” values  $\tilde{\theta}'$  are generated by sampling from a normal distribution with variance proportional to  $\tilde{\rho}^{-1}$ , mimicking the typical scaling of parameter errors with inverse SNR. Posterior samples  $\hat{\theta}'$  are obtained by further drawing from normal distributions centred at  $\tilde{\theta}'$  with variances also proportional to  $\tilde{\rho}^{-1}$ . The  $\{\tilde{\theta}', \tilde{\rho}\}$  samples are then transformed back into  $\{\hat{\theta}', \hat{D}_L\}$  samples via Eq. (B.1). The proportionality constants for the measurement errors on  $\theta'$  were calibrated against mock parameter estimation runs.

The problem can be simplified by noting that the SNR may be expressed as

$$\rho = \rho_{\text{opt}} \Theta, \quad (\text{B.2})$$

where  $\rho_{\text{opt}}$  is the optimal SNR for a source located directly overhead the detector with face-on inclination, and  $\Theta$  encodes the dependence on sky location, polarisation, and inclination. For a single detector,  $\Theta$  is bounded by  $0 \leq \Theta \leq 1$ , while for ET the range becomes  $0 \leq \Theta_{\text{ET}} \leq \sqrt{3}$ . Denoting by  $F_{+,i}$  and  $F_{\times,i}$  the antenna pattern functions of the three equivalent ET detectors, as given in Regimbau et al. (2012), the factor  $\Theta_{\text{ET}}$  can be written as

$$\Theta_{\text{ET}} = \sqrt{\sum_{i=1}^3 (F_{+,i}^2 + F_{\times,i}^2)}. \quad (\text{B.3})$$

This expression generalises the single-detector relation derived in Finn & Chernoff (1993), but is strictly valid only for the case of a triangular ET configuration, where all three detectors are co-located. We note that in a network of multiple detectors, the distribution of the measured SNR,  $\hat{\rho}$ , deviates slightly from the simple normal form assumed in the single-detector case (Essick 2023; Gerosa & Bellotti 2024). However, for the purposes of this study, we neglect this correction and adopt the single-detector approximation for simplicity.

Our approach differs from that of Fishbach et al. (2020); Farah et al. (2023) in two main respects. First, although we enforce hard prior boundaries when drawing the posterior samples  $\hat{\theta}'$ , we do not impose such constraints when generating the “noisy” parameter values  $\tilde{\theta}'$ . This choice reflects the fact that noise can make it appear as the likelihood peaks outside of the prior limits, which manifests as railing of the posterior against the prior boundary. This is also simpler, as it means that the likelihood is truly a Gaussian and not a truncated Gaussian, avoiding the need to adjust the sampling procedure to account for a modified functional form.

Second, Fishbach et al. (2020); Farah et al. (2023) adopt  $\theta' = (\mathcal{M}_{c,d}, \eta, \Theta)$  as sampling parameters, where  $\mathcal{M}_{c,d}$  is the detector-frame chirp mass and  $\eta$  is the symmetric mass ratio. However, we find that sampling in the symmetric mass ratio leads to large variances in the Monte Carlo estimators used when evaluating the population likelihood (see App. D). This issue arises because our underlying population model favours nearly equal-mass systems, while sampling in  $\eta$  tends to underpopulate the region near  $q \sim 1$ , as also discussed in Farah (2022). To mitigate this, we sample directly in the mass ratio  $q$  instead of  $\eta$ . We assume that uncertainties in the inferred mass ratio scale as  $0.15\rho_{\text{th}}/\rho$ , which is a conservative estimate based on the measurement uncertainties reported for GW170817 (Abbott et al. 2017) and GW190425 (Abbott et al. 2020), particularly when tight spin priors are used. Although the mapping from detector-frame chirp mass to total mass is less problematic, we likewise choose to sample directly in the detector-frame total mass, adopting a similarly conservative uncertainty scaling of  $0.1\rho_{\text{th}}/\rho$ . For  $\Theta$  we use the same as Fishbach et al. (2020); Farah et al. (2023):  $0.21\rho_{\text{th}}/\rho$ .

SNRs are computed using the GWBENCH package (Borhanian 2021), setting the spins to 0 and using the IMRPhenomXHM waveform (García-Quirós et al. 2020). For the SNR threshold, we take  $\rho_{\text{th}} = 8$ .

## Appendix C: Hierarchical Bayesian analysis

We denote with  $\theta$  the set of parameters describing a GW event,  $p(d|\theta)$  the single event likelihood and  $p(\theta|\Lambda)$  the population prior on  $\theta$ , which depends on hyperparameters  $\Lambda$  that we wish to infer. The population likelihood for observing  $N_{\text{obs}}$  events  $\{d\} = \{d_1, \dots, d_{N_{\text{obs}}}\}$ , marginalised over the event rate is Mandel et al. (2019); Vitale et al. (2020)

$$p(\{d\}|\Lambda) = \prod_i^{N_{\text{obs}}} \int \frac{p(d_i|\theta)p(\theta|\Lambda)}{p_{\text{det}}(\Lambda)} d\theta. \quad (\text{C.1})$$

We have introduced the selection function defined via

$$p_{\text{det}}(\Lambda) = \int p_{\text{det}}(\theta)p(\theta|\Lambda) d\theta, \quad (\text{C.2})$$

$$p_{\text{det}}(\theta) = \int_{d>\text{threshold}} p(d|\theta) dd, \quad (\text{C.3})$$

where the second integral is restricted to realisations  $d$  that exceed the detection threshold (defined via the chosen ranking statistic), here the measured matched filter SNR  $\hat{\rho}$ .

Alternatively, if we do not wish to marginalise over the rate, we can write

$$p(\{d\}|\Lambda) = e^{-N(\Lambda)p_{\text{det}}(\Lambda)} \prod_i^{N_{\text{obs}}} \int p(d_i|\theta) \frac{dN}{d\theta}(\Lambda) d\theta. \quad (\text{C.4})$$

where  $\frac{dN}{d\theta}$  is the differential number of events,  $N(\Lambda) = \int \frac{dN}{d\theta}(\Lambda) d\theta$  is the total expected number of events, and we have the relation  $\frac{dN}{d\theta} = N(\Lambda)p(\theta|\Lambda)$ .

In practice, the single-event likelihood can be written in terms of the posterior and the parameter estimation prior via Bayes’ theorem. The integral over  $\theta$  is evaluated using Monte Carlo integration, based on posterior samples obtained as described in App. B.

Similarly, the selection function is estimated via an injection campaign in which events are drawn from an injection distribution  $\pi_{\text{inj}}(\theta)$ , and only those satisfying the detection criterion are retained, forming the set  $\theta_{\text{det}}$ . The detection probability is then computed using importance sampling:

$$p_{\text{det}}(\Lambda) = \sum_{\theta_{\text{det}}} \frac{p(\theta_{\text{det}} | \Lambda)}{\pi_{\text{inj}}(\theta_{\text{det}})}. \quad (\text{C.5})$$

As discussed in Talbot & Golomb (2023), the finite number of samples used to evaluate the integrals in population analyses can introduce significant variance in the Monte Carlo estimators, which may in turn lead to biases. To mitigate this issue in the estimation of the selection function, we choose the injection prior to match the true population, thereby reducing the variance in the importance sampling weights. Additionally, in line with the recommendations of Talbot & Golomb (2023), we impose a threshold on the total variance of the log-likelihood and discard hyperparameters exceeding this limit.

The posterior on  $\Lambda$  is then obtained through Bayes’ theorem:  $p(\Lambda|\{d\}) \propto p(\{d\}|\Lambda)\pi(\Lambda)$ , with the priors described in Sec. 2 and in the next one. The sampling is performed with the Eryn sampler<sup>2</sup> (Karnesis et al. 2023).

## Appendix D: Reconstruction of the mass distribution

Figure 1 shows representative examples of how the measurement of the total mass and the mass ratio distribution improves as the number of events increases. These plots correspond to realisations of the  $\alpha_L = 1$  case; however, the choice of  $\alpha_L$  has little impact on this result.

<sup>2</sup> Publicly available at <https://github.com/mikekatz04/Eryn>.

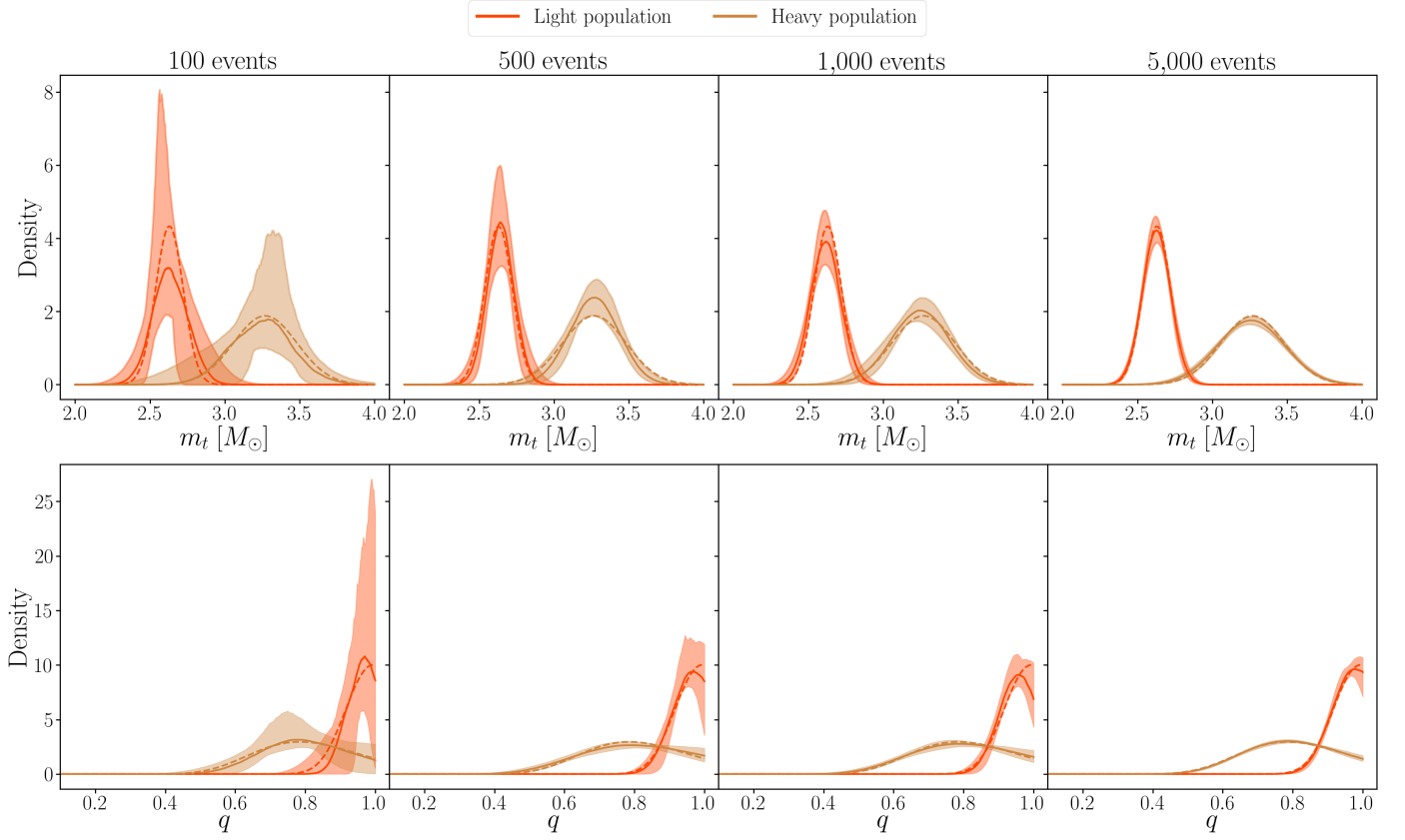


Fig. 1: Reconstructions of the total mass and mass ratio distributions for increasing catalogue sizes. Coloured bands show the 90% credible intervals for the light (red) and heavy (golden) populations. Solid lines indicate the median reconstructions, while dashed lines mark the true distributions.